Silicon chip integrated Photonic Sensors for Biological and Chemical Sensing

Swapnajit Chakravarty[a], Yi Zou[b], Hai Yan[b], Naimei Tang[b], Ray T. Chen*[a,b],

[a]Omega Optics Inc., 8500 Shoal Creek Blvd. Bldg. 4, Suite 200, Austin, TX, USA 78757;
[b]Dept. of Electrical and Computer Engineering, University of Texas, 10100 Burnet Road Bldg. 160, Austin, TX USA 78758

ABSTRACT

We experimentally demonstrate applications of photonic crystal waveguide based devices for on-chip optical absorption spectroscopy for the detection of chemical warfare simulant, triethylphosphate as well as applications with photonic crystal microcavity devices in the detection of biomarkers for pancreatic cancer in patient serum and cadmium metal ions in heavy metal pollution sensing. At mid-infrared wavelengths, we experimentally demonstrate the higher sensitivity of photonic crystal based structures compared to other nanophotonic devices such as strip and slot waveguides with detection down to 10ppm triethylphosphate. We also detected 5ppb (parts per billion) of cadmium metal ions in water at near-infrared wavelengths using established techniques for the detection of specific probe-target biomarker conjugation chemistries.

Keywords: photonic crystal waveguide, on-chip absorption spectroscopy, photonic crystal microarray, biosensor.

1. INTRODUCTION

Over the last decade, lithography advances have seen the development of photonic nano and microstructures with applications in chemical and biological sensing. Various devices have been demonstrated in the context of sensing including strip waveguides [1], Mach-Zehnder interferometers [2], ring resonators [3], gratings [4] and surface plasmon resonance [5] devices. The promise of lab-on-chip sensors received a tremendous boost with the advent of artificial dielectric structures called photonic crystals with high sensitivity to refractive index changes that promise SWAP (size, weight and power) and cost benefits highly desired for integrated photonic sensing.

During the past few years, we have developed a photonic crystal (PC) open sensor chip-integrated platform for high throughput low cost optical sensing with high sensitivity and selectivity with projected applications in environmental sensing, biomedical sensing, as well as explosives detection, chemical warfare agents detection for national security [6-10]. Silicon based devices are proposed as the generic platform for the development of these devices due to its mature processing technology which makes it amenable for cost-effective high volume production. For on-chip optical absorption spectroscopy, our slotted photonic crystal waveguide (SPCW) based sensor showed significantly higher sensitivity than strip and slot waveguides and detected chemical warfare agents in the mid-infrared (mid-IR) by absorbance signatures, taking advantage of larger absorption cross-sections of molecules [11-13]. In on-chip biosensing, we continued our research in sensors comprising PC microcavity devices coupled to PCWs for new applications in pancreatic cancer biomarker detection, and metal pollution sensing in water.

2. ON-CHIP ABSORPTION SPECTROSCOPY

Infrared (IR) spectroscopy is widely used as a simple and reliable technique for quality control and analysis. Due to the fact that infrared spectroscopy does not require costly analyte labeling, the technique is very attractive for sensing and identification compared to other spectroscopy methods. Commercially available optical absorption spectrometers are mostly large, heavy, power consuming and expensive. Furthermore, they can detect only a few species at a time. Systems that detect multiple species are prohibitively expensive and not portable.

---

*raychen@uts.cc.utexas.edu; phone 1 512-471-7035; fax 1 512-471-8575; bart.mer.utexas.edu:16080/Chen/optic-inter/

Infrared absorption spectroscopy is based on the Beer-Lambert law. According to this technique, transmitted intensity I is given by:

$$I = I_0 \exp(-\gamma \alpha L) \quad \ldots\ldots (1)$$

where I_0 is the incident intensity, α is the absorption coefficient of the medium, L is the interaction length and γ is the medium-specific absorption factor determined by dispersion enhanced light-matter interaction. In conventional free-space systems, $\gamma = 1$; thus L must be large to achieve a suitable sensitivity of measured I/I_0. Various complex schemes have been demonstrated to increase absorption path lengths, present state-of-the-art dimensions are still significantly large to be accommodated on a semiconductor chip.

For lab-on-chip systems, L must be small, hence γ must be large. It was shown in Ref. [14] using perturbation theory that

$$\gamma = f \times \frac{c/n}{v_g} \quad \ldots\ldots (2)$$

where c is velocity of light in free space, v_g is group velocity in medium of effective index n and f is filling factor denoting relative fraction of optical field residing in the analyte medium. Equation 2 shows that slow light propagation (small v_g) significantly enhances absorption. Furthermore, greater the electric field overlap with the analyte, greater the effective absorption by the medium. Both conditions of small v_g and high f are fulfilled in a PC slot waveguide [6, 7].

While silicon is chosen as the waveguiding core for operation both in the near-IR and mid-IR, our structures employ a lower cladding to provide large mechanical support to the waveguide devices, to enable operation in harsh environments. Silicon dioxide (SiO_2) employed as bottom cladding in the near-IR is transparent till $\lambda=3.7\mu m$. Silicon is optically transparent till $\lambda\sim8\mu m$. To develop an optical platform applicable more broadly across the mid-IR, a silicon-on-sapphire (SoS) platform is used for lab-on-chip mid-IR absorption spectroscopy.
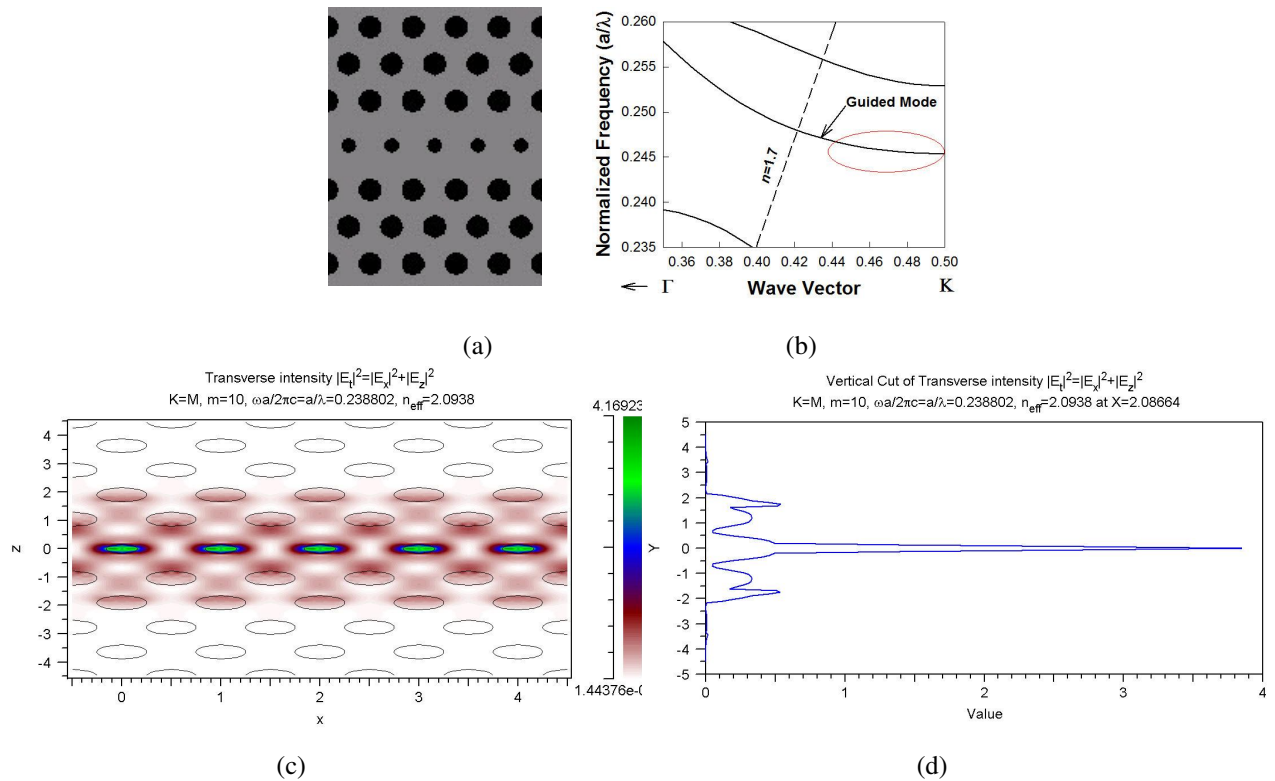
3. DEVICE DESIGN FOR MID-IR ON-CHIP SPECTROSCOPY

(a)   (b)

(c)   (d)

Fig. 1. (a) Schematic of the holey W1.2 PCW with a row of smaller air holes with radius $rs=0.625r$, in the center of the PCW. (b) Dispersion diagram of the device in (a) by plane-wave expansion. (c) Electric field intensity profile of the propagating slow light at the Brillouin zone boundary mode shown by dashed circle in (b). (d) Cross-section of the electric field intensity in (c) profile through the smaller air holes in the center of the PCW. [11]

A schematic of the holey PCW is shown in Fig. 1(a). The holey PCW device comprised a W1.2 PCW with a single missing row of holes along the Γ−K direction in a hexagonal lattice of air holes in silicon, with lattice constant a. At the center of the PCW, a row of smaller holes with radius $rs=0.625r$, where $r=0.25a$ is the radius of the holes in the bulk lattice, is etched at the lattice positions of the PC. W1.2 indicates that the width of the PCW at the onset of the taper is $1.2× \sqrt{3}a$. Fig. 1(b) shows the dispersion diagram of the holey PCW obtained by 2D plane-wave expansion simulation using effective index $n=2.91$. The dispersion diagram shows the guided mode separated from the dielectric band by a stop gap. The light line for sapphire is superimposed. The electric field intensity profile of the propagating slow light mode, indicated by the red circle in Fig. 1(b) is shown in Fig. 1(c). Fig. 1(d) is a cross section of the field intensity profile in Fig. 1(c) through one of the holes in the center of the holey PCW, showing the factor of 4 enhancement in the electric field intensity in the holes.

Another structure investigated is the slotted PCW shown in Fig. 2(a). The slotted PCW device comprises a W1.5 PCW with a single missing row of holes along the Γ−K direction in a hexagonal lattice of air holes in silicon, with lattice constant a. The radius of air holes is $r=0.25a$. At the center of the PCW, a rectangular slot with width $s=0.155a$, is etched from the input to the output. W1.5 indicates that the width of the PCW at the onset of the taper is $1.2× \sqrt{3}a$. Fig. 2(b) shows the dispersion diagram of the holey PCW obtained by 3D plane-wave expansion simulation. The electric field intensity profile of the propagating slow light mode, indicated by the dashed circle in Fig. 2(a) is shown in Fig. 2(c). Fig. 2(d) is a cross section of the field intensity profile in Fig. 2(c), showing the factor of 13 enhancement in the electric field intensity in the slot, larger than the holey PCW.
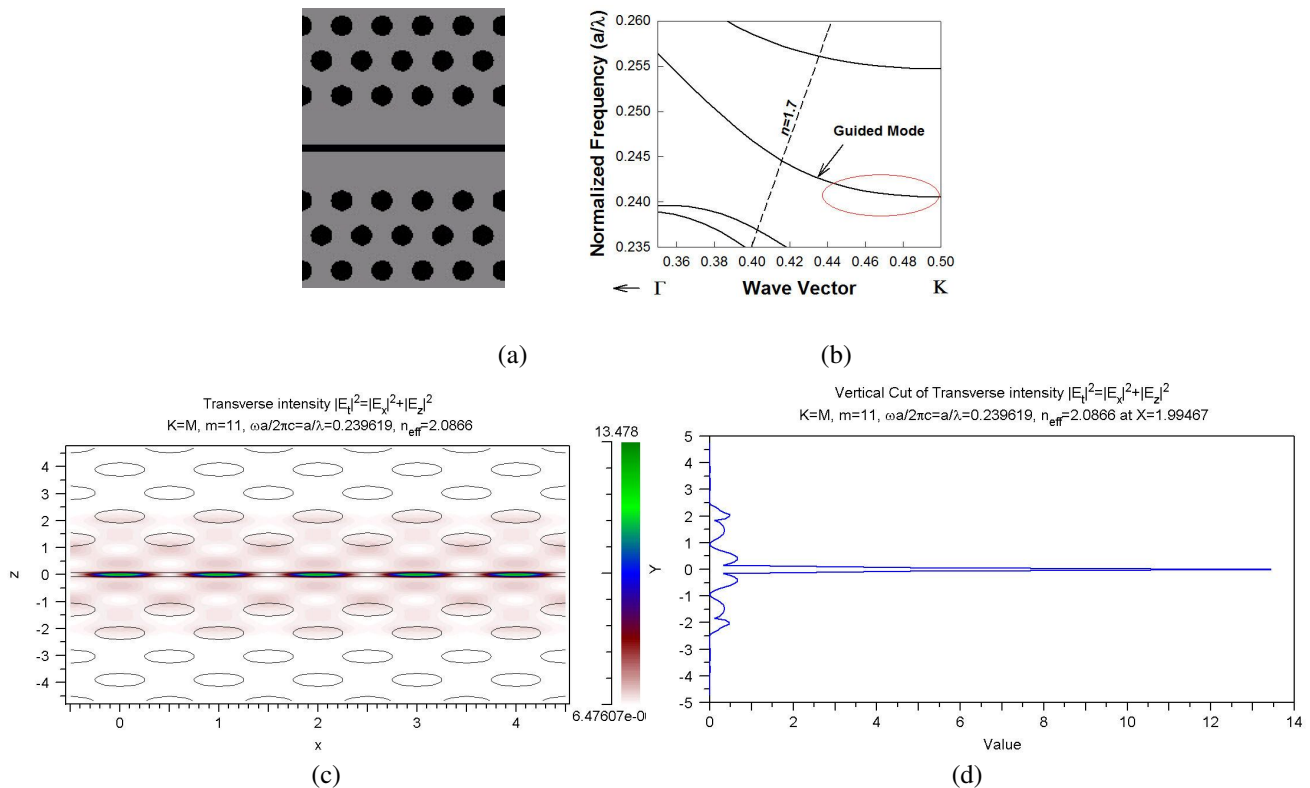

(a)

(b)

(c)

(d)

Fig. 2. (a) Schematic of the slotted W1.5 PCW with a rectangular slot $s=0.155r$, in the center of the PCW. (b) Dispersion diagram of the device in (a) by plane-wave expansion. (c) Electric field intensity profile of the propagating slow light mode at the Brillouin zone boundary shown by dashed circle in (b). (d) Cross-section of the electric field intensity profile in (c). [11]

Figs. 3 (a) and 3(b) show the electric field intensity profile and the cross-section intensity in a conventional W1 PCW. In contrast to the holey and slotted PCWs, the electric field intensity is primarily located in the dielectric (silicon in this case) and only interacts evanescently in-plane with the holes adjacent to the PCW.

Transverse intensity $|E_t|^2=|E_x|^2+|E_z|^2$
K=M, m=10, $\omega a/2\pi c=a/\lambda=0.241322$, $n_{eff}=2.0719$

Vertical Cut of Transverse intensity $|E_t|^2=|E_x|^2+|E_z|^2$
K=M, m=10, $\omega a/2\pi c=a/\lambda=0.241322$, $n_{eff}=2.0719$ at X=1.99467
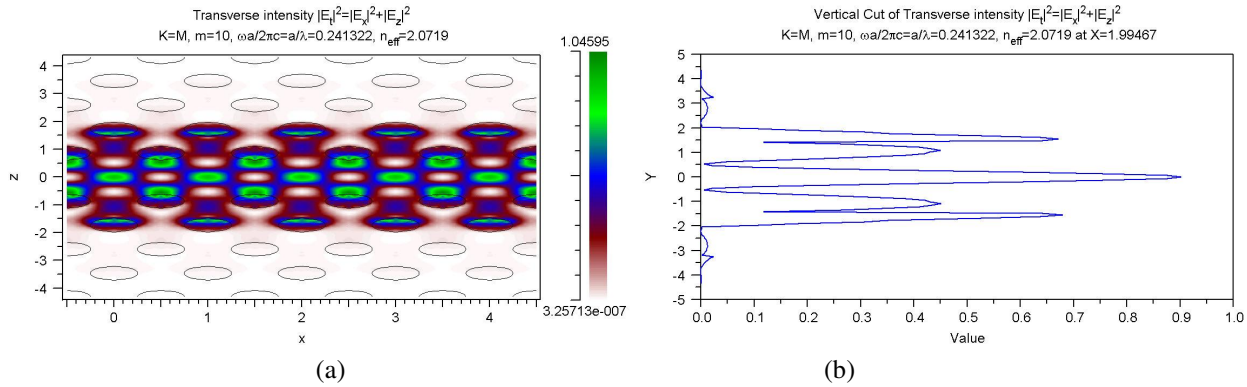
(a)   (b)

Fig. 3. (Color online) (c) Electric field intensity profile of the propagating slow light mode in a W1 PCW at the Brillouin zone boundary. (d) Cross-section of the electric field intensity profile in (c). [11, 12]

4. EXPERIMENTAL RESULTS

The height of the silicon device layer was determined to be h=585 +/-1nm from ellipsometry for the holey PCW and h=575 +/-1nm from ellipsometry for the slot PCW with mean square error (MSE) equal to 6Å. h/a of the silicon slab was calculated accordingly for each lattice constant. Devices were fabricated using a combination of electron beam lithography and inductively coupled plasma etching. Scanning electron micrograph (SEM) images of the devices are shown in Fig. 4 and Fig. 5 respectively.
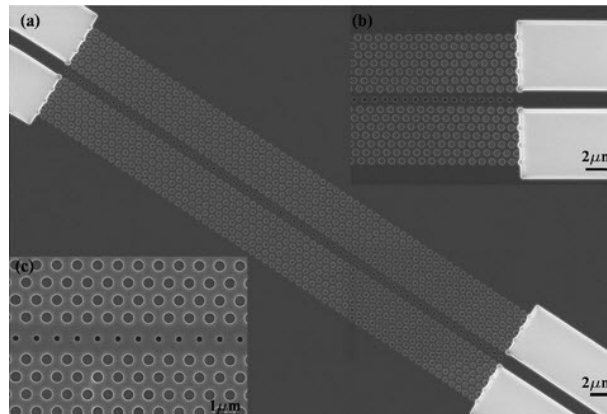

Fig. 4. (a) SEM image of the holey PCW. Top view magnified images showing the holey PCW (b) near the center of the device in (a) and (c) at the interface between the PCW and the input ridge waveguide. [11]

Light at 3.43µm from a source Thorlabs ICL is coupled into and out of the chip from a single mode ZrF_4 fiber from Thorlabs using subwavelength grating (SWG) couplers. The design and characterization of SWGs used has been described in detail in Ref. [13]. A PC group index taper is implemented at the input and output interfaces of the holey PCW with the ridge waveguide to reduce Fresnel reflection losses and enhance light coupling efficiency into the slow light guided mode. The PC group index taper is formed by gradually widening the PCW from W1.2 to W1.27 at the interface between the strip waveguide and holey PCW. All device components for the respective holey and slotted PCWs are fabricated in the same step and post-processed as described before in Piranha/HF [11-13].

The light from the output SWG for short 50µm (~60 periods) long holey PCW devices with several lattice constants but the same r/a is plotted in Fig. 5(a). The length of the W1 PCW is 50 µm. The plot is normalized with respect to the highest and lowest power observed versus lattice constant. It is observed that for a less than 830nm, the output power from the devices is practically zero. Propagation loss measurements were done for several devices in Fig. 6(a) and plotted. Devices with lengths 50µm, 100µm, 200µm and 400µm were fabricated at a=840nm, 845nm, 850nm, 865nm, 870nm and 890nm. Transmission losses as observed in Fig. 5(b) were obtained. The lattice constants for propagation loss characterization were chosen based on a comparison with previous data in Ref. [12] which showed a similar bulge

in the short 50µm long PCWs at lattice constants for which the ICL emission propagates at wavelengths near the light line boundary. It was ensured from ellipsometry that the selected chips for fabrication had h=585nm +/-1nm with mean square error (MSE) equal to 6Å. Fig. 5(a) also plots the corresponding propagation losses versus lattice constant (open circles). The measured propagation losses at a=840nm and 845nm are 15dB/cm and 13dB/cm respectively. At a=850nm, a=865nm, a=870nm, and a=890nm, the propagation loss increases rapidly with increasing length of the PCW, reaching as high as 900dB/cm for a=890nm. It can thus be concluded that the ICL emission propagates above the light line for devices with a greater than 845nm. The stop gap and light line boundaries are thus approximately demarcated based on the transmission measurements. In between the two dashed line, light propagates in the holey PCW mode below the light line. As the lattice constant is decreased, from left to right in the inset of Fig. 5(a), the ICL emission propagates in the respective devices at higher group indices as a result of which the propagation loss increases and the transmitted intensity decreases.
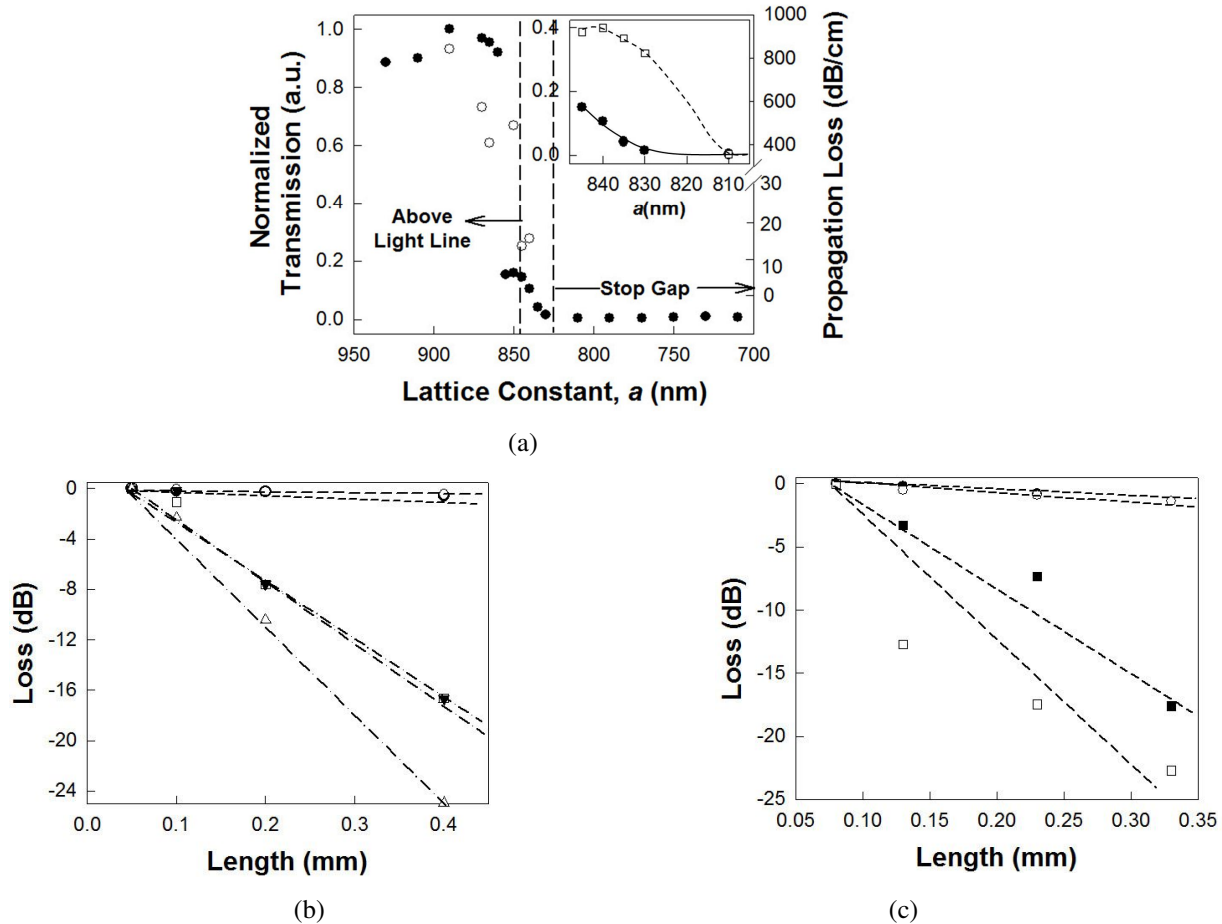

(a)

(b)

(c)

Fig. 5. (a) Normalized transmitted intensity through an air-clad W1.2 holey PCW in SoS with r=0.25a, rs=0.625r as a function of a at λ=3.43µm plotted in air (bold circles). Propagation losses were measured for few devices (open circles). Insets magnify the data for devices between a=810nm and a=845nm in air (●) and tetrachloroethylene (□). (b) Propagation loss for devices of different length at a=840nm (●), a=845nm (○), a=850nm (□), a=865nm (■)and a=870nm (▲). (c) (b) Propagation loss for devices of different length at a=830nm (●), a=840nm (○), a=850nm (■) and a=860nm (□) in a slotted PCW with rectangular slots.

Fig. 5(c) plots the propagation loss from the slotted PCW. Similar to the holey PCW, zero transmission is observed for lattice constants for which our single wavelength laser source at 3.43µm propagates in the stop gap of the dispersion diagram. High propagation losses exceeding 600dB/cm are observed for representative lattice constants a=850nm and a=860nm for which the single wavelength at 3.43µm propagates above the sapphire light line. Significantly lower propagation losses are observed at representative lattice constants a=830nm and a=840nm when the single wavelength source is propagated by the guided mode in the PCW slot waveguide.

We observe that the guided mode propagation loss below the light line for the PC slot waveguide device including the input and output mode converter, while still significantly lower than above the light line, is of the order of 55dB/cm. In the near-infrared, wide-slotted silicon PC slot waveguides in silicon-on-insulator (SOI) have demonstrated propagation losses of the order of 30dB/cm. Narrow slotted PC slot waveguides in SOI comparable to the scaled slot width in the present case have demonstrated similar propagation losses as those demonstrated here.

Since the propagation losses for the holey PCW were significantly lower than that for the slotted PCW, hence holey PCW devices were selected for the detection of TEP by optical absorbance at 3.43μm. The transmitted light through an 800μm long holey PCW with a=845nm is measured in the presence and absence of TEP. A measured quantity of TEP was provided by controlling the gas flow-rate in a commercial Kin-tek vapor generator. And the vapor released via heated tubing at a height of approximately 2-3mm from the surface of the chip to mimic a field version of the system with gas being sensed in free space. The chip surface was also heated to 70°C to ensure that the vapors of TEP did not condense onto the surface of the chip. Fig. 6 shows the change in transmitted light intensity through the holey PCW with instantaneous switching on and switching off of the TEP flow at 10ppm. The transmitted signal intensity does not drop instantaneously, instead takes about 300 seconds to reach the steady state in the presence of TEP.
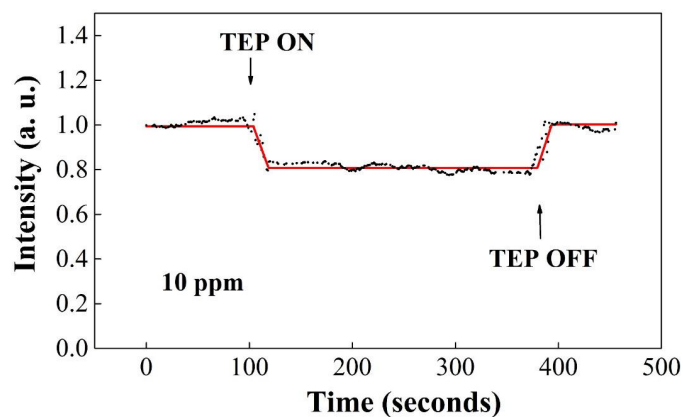

Fig. 6: Change in transmitted intensity through an 800μm long holey slotted photonic crystal waveguide in the presence and absence of 10ppm TEP. [11]

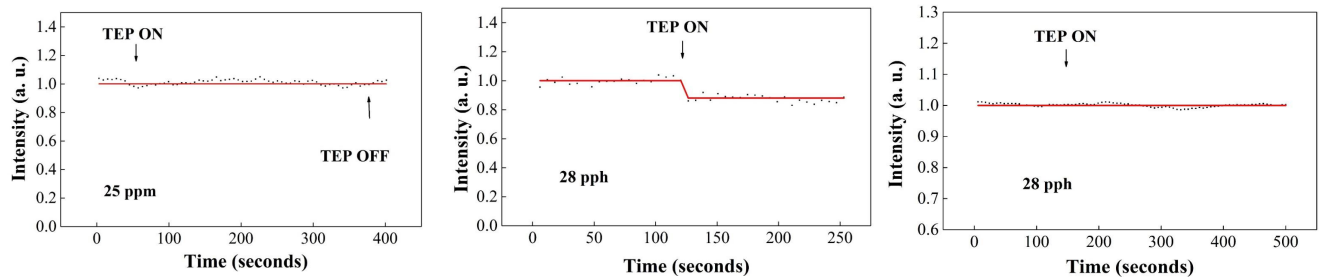## 5. DISCUSSION ON ON-CHIP ABSORPTION SPECTROSCOPY

Fig. 7: Transmitted light intensity through a slot waveguide in the presence and absence of (a) 25ppm TEP and (b) 28pph TEP. (c) Transmitted light intensity through a strip waveguide in the presence and absence of 28pph TEP [11].

When the holey PCW section in Fig. 6 is replaced by a slot waveguide between the input and output SWGs, no change in intensity of light transmitted at 3.43μm is observed at 25ppm TEP concent ration in Fig. 7(a), while a small change in intensity is observed at a much larger TEP concentration of 28pph in Fig. 7(b). When the holey PCW section in Fig. 6 is replaced by a strip waveguide, no change in transmitted intensity is observed at 28pph TEP in Fig. 7(c).

The results clearly indicate the benefit of slow light and filling fraction from Eq. 1 and Eq. 2 and provide a pathway towards the realization of lab-on-chip optical absorption spectroscopy in the entire infrared bandwidth. The attractiveness of the photonic crystal open sensor platform thus resides in the ready extension of one single design scaled

in lattice constant on the normalized photonic band dispersion curve to any wavelength to achieve the detection of the necessary analyte with high sensitivity.

6. CHEM-BIO MICROARRAYS

A second application of the photonic crystal open sensor platform in silicon is in microarrays. Microarrays provide an unprecedented opportunity for comprehensive concurrent analysis of thousands of biomolecules such as proteins [15], genes [16], DNA molecules [17], small molecules [18] or nucleic acids [19]. During the past 6 years, we have demonstrated several biosensor devices with applications in the detection of biomarkers for lung cancer [8], and pancreatic cancer [20]. We have also demonstrated applications in therapeutic drug monitoring via the detection of small molecule antibiotics [21] and also in the detection of metal pollutants in water [22].

The device consists of a triangular lattice of air holes etched into silicon in a silicon-on-insulator (SOI) substrate. Photonic crystal waveguides are defined and photonic crystal microcavities with different geometries are fabricated at specific intervals along the length of the photonic crystal waveguide. The resonant wavelength of a photonic crystal microcavity is dependent on the geometry of the microcavity. Light propagating in a photonic crystal waveguide couples to a photonic crystal microcavity at the resonant wavelength of the microcavity. The transmission spectrum of the photonic crystal waveguides consequently shows minima corresponding to the resonant wavelength of each photonic crystal microcavity. Target proteins for bio-agents and pathogens, each specific to a unique probe molecule for diagnostic distinction, are patterned on a unique microcavity using a fabrication technique that preserves the protein functionality. When a probe molecule binds with its specific target, the resonant wavelength of that microcavity shifts which consequently shifts the corresponding minimum in the waveguide transmission spectrum. The shift in the minimum in the transmission spectrum identifies the occurrence of a binding event. The magnitude of binding is determined by De Feijter's formula [23] that relates the absolute amount of adsorbed molecules M with the change in refractive index as:

$$M = d_A \frac{n_A - n_C}{dn/dc}$$

where d_A is the thickness of adsorbed layer, n_A is the refractive index of adsorbed molecules, n_C is the refractive index of cover solution and dn/dc is the change in refractive index of molecules which is proportional to the shift dλ in position of the resonance peak [24]. The magnitude of resonant wavelength shift is proportional to the amount of adsorbed biomolecules and hence provides a label-free means to quantitatively determine biomolecules of interest.
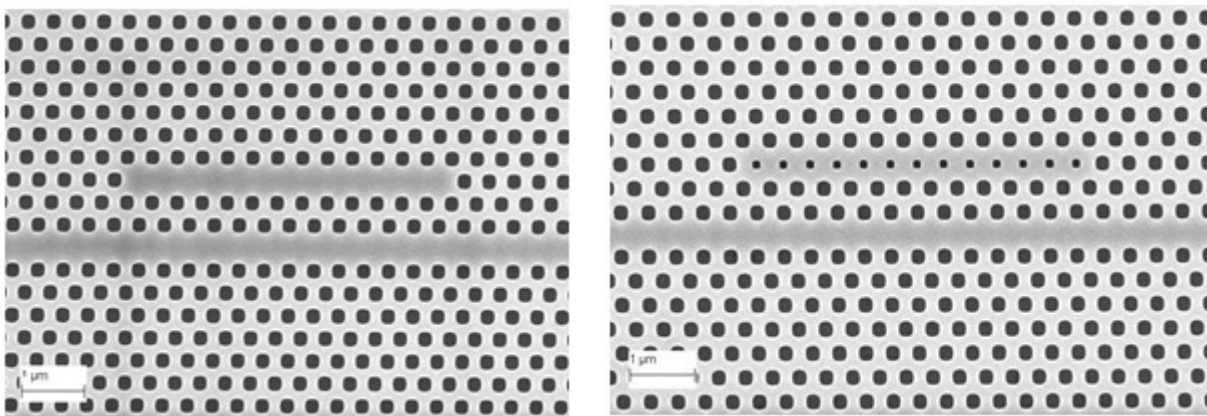

Fig. 8. SEM images of photolithographically fabricated devices from a commercial foundry. (a) L13 PC microcavity coupled to a W1 PCW. (b) 13 PC microcavity with nanoholes, which is coupled to a PCW.

Details of device design and fabrication have been covered extensively before and are not repeated here. We studied the dependence of device sensitivity on various factors such as cavity quality factor, cavity mode volume, slow light, fill fraction and analyte absorbance [25-28]. In the following section, we summarize some of our recent results in different applications, where we compared the sensitivities of two PC cavities, a L13 type PC cavity as shown in Fig. 8(a) and a L13 PC cavity with nanoholes as shown in Fig. 8(b).
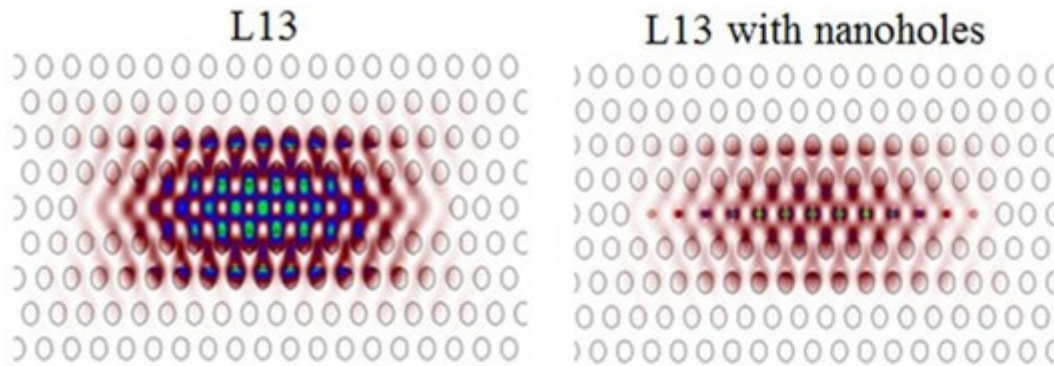
Fig. 9. Electric field intensity profiles of (a) L13 PC microcavity without nanoholes versus (b) L13 PC microcavity with nanoholes showing the field concentration in the nanoholes.

The L13 PC microcavity with nanoholes had a larger analyte fill fraction as seen from the electric field profiles in Figs. 9(a) and 9(b) respectivly. Our results showed higher sensitivity of the L13 PC microcavity with nanoholes compared to other microcavity devices.

7. EXPERIMENTAL RESULTS

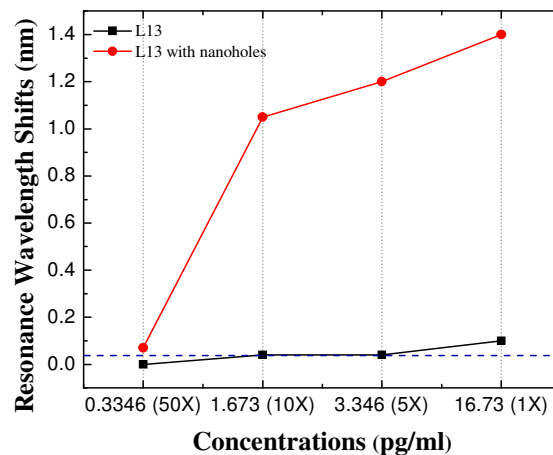### 7.1. Chip-Integrated detection of pancreatic cancer biomarkers

Fig. 10. Plot showing the enhanced sensitivity of L13 with nanohole type of PC microcavity versus conventional L13 PC microcavity, with respect to detection of pancreatic cancer biomarkers.

Two dimensional photonic crystal microcavities were fabricated by photolithography and their respective sensitivities to biomarkers in patient serum samples were compared for different microcavity characteristics of quality factor and analyte fill fraction. Three different biomarkers in plasma from pancreatic cancer patients were experimentally detected by conventional L13 PC microcavities without nanoholes and higher sensitivity L13 PC microcavities with nanoholes. 8.8 femto-molar (0.334pg/ml) concentration of pancreatic cancer biomarker in patient plasma samples was experimentally detected at 50 times dilution than ELISA in a PC microcavity with high quality factor and high analyte fill fraction. A higher sensitivity was observed, as expected with a L13 PC microcavity with nanoholes versus the L13 PC microcavity without nanoholes due to the higher overlap integral in the former. Details are covered in ref. [20].

7.2. Chip-Integrated detection of heavy metals in water

Heavy metal ions released into the environment from industrial processes lead to various health hazards. We demonstrated an on-chip label-free detection approach that allows high-sensitivity and high-throughput detection of heavy metals. 2D PC microcavities were combined by MMI to form a sensor array. We experimentally demonstrated the detection of cadmium-chelate conjugate with concentration as low as 5 parts-per-billion (ppb) [22] As observed from Fig. 11, the L13 PC microcavity with nanoholes showed a larger resonance wavelength shift for the same concentration of metal ions than the L13 PC microcavity without nanoholes.
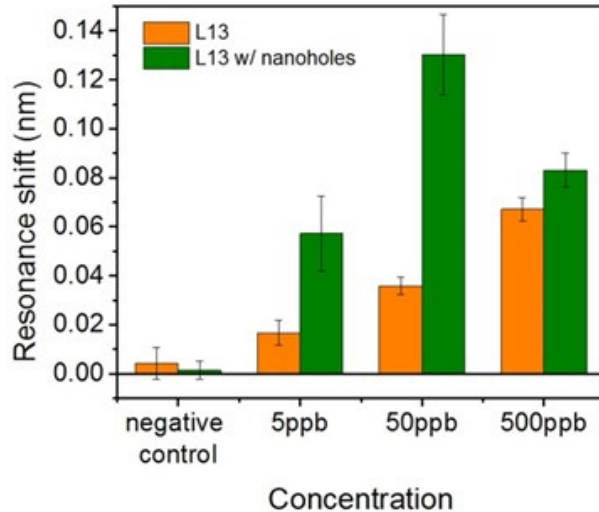

Fig. 11: Resonance shift of the L13 and L13 with nanoholes PC biosensor after applying increasing concentration of cadmium metal ions in water.

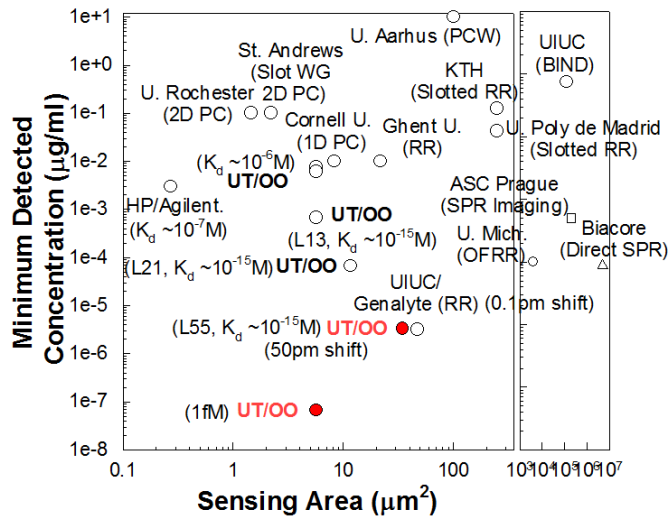# 8.   DISCUSSION ON ON-CHIP MICROARRAY SENSITIVITY

Fig. 12: Chart comparing minimum detection limits of PC microcavity based biosensors versus other label-free optical platforms as a function of sensing area on chip.

Fig. 12 summarizes the sensitivities and detection limits demonstrated in PC microcavities compared to other label-free methods, including surface plasmon resonance devices [5], opto-fluidic ring resonators [29], ring resonator [3, 30-32] and other photonic crystal (PC) devices [33-38] and grating devices [39] as function of sensing area. The sensitivities as a function of dissociation constant is also reflected in this figure. The PC devices thus demonstrated the highest sensitivities amongst existing chip-integrated nanophotonic sensing technologies

9. SUMMARY

In summary, we have demonstrated two typical devices on the photonic crystal open sensor platform, both on silicon, one for chip-integrated absorption spectroscopy and the other for chip-integrated biomolecular microarray assays. We have demonstrated the higher sensitivity of devices on the photonic crystal platform compared to other nanophotonic devices, in both cases of lab-on-chip absorption spectroscopy and lab-on-chip biological and chemical sensing. Diverse applications in environmental sensing, explosive detection for national security, bio-sensing for microbial contamination, food and beverage protection, various cancer detections can be envisioned on a single platform..

REFERENCES

[1] Densmore, A., Vachon, M., Xu, D.X., Janz, S., Ma, R., Li, Y. H., Lopinski, G., Delage, A., Lapointe, J., Luebbert, C. C., Liu, Q. Y., Cheben, P., and Schmid, J. H., "Silicon photonic wire biosensor array for multiplexed real-time and label-free molecular detection", Opt. Lett. 34(23), 3598 (2009).

[2] Luff, B.J., Wilkinson, J. S., Piehler, J., Hollenbach, U., Ingenhoff, J., and Fabricius, N., "Integrated Optical Mach–Zehnder Biosensor", J. Lightwave Tech. 16(4), 583 (1998).

[3] Iqbal, M., Gleeson, M.A., Spaugh, B, Tybor, F., Gunn, W.G., Hochberg, M., Baehr-Jones, T., Bailey, R.C., and Gunn, L.C., "Label-Free Biosensor Arrays based on silicon ring resonators and high-speed optical scanning instrumentation", IEEE Journal of Selected Topics in Quantum Electronics 16(3), 654 (2010)

[4] Fang, Y., Ferrie, A. M., Fontaine, N. H.., Mauro, J., and Balakrishnan, J., "Resonant Waveguide Grating Biosensor for Living Cell Sensing", Biophys. J. 91(5), 1925 (2006).

[5] Sipova, H., Zhang, S., Dudley, A. M., Galas, D., Wang, K., and Homola, J., "Surface plasmon resonance biosensor for rapid label-free detection of microribonucleic acid at subfemtomole level", Anal. Chem. 82, 10110 (2010).

[6] Lai, W-C., Chakravarty, S., Wang, X., Lin, C-Y., and Chen, R. T., "Photonic crystal slot waveguide absorption spectrometer for on-chip near-infrared spectroscopy of xylene in water", Appl. Phys. Lett. 98(2), 023304 (2011).

[7] Lai, W-C., Chakravarty, S., Wang, X., Lin, C-Y., and Chen, R. T., "On-Chip methane sensing by near-IR absorption signatures in a photonic crystal slot waveguide", Optics Lett. 36 (6), 984 (2011).

[8] Chakravarty, S., Lai, W-C., Zou, Y., Drabkin, H.A., Simon, G.R., Chin, S.H., Gemmill, R. M., and Chen, R.T., "Multiplexed Specific Label-Free Detection of NCI-H358 Lung Cancer Cell Line Lysates with Silicon Based Photonic Crystal Microcavity Biosensors," Biosensors and Bioelectronics 43, 50 (2013).

[9] Lai, W-C., Chakravarty, S., Zou, Y., and Chen, R.T., "Silicon nano-membrane based photonic crystal microcavities for high sensitivity bio-sensing," Optics Letters 37 (7), 1208 (2012).

[10] Zou, Y., Chakravarty, S., Lai, W-C., and Chen, R.T., "Methods to Array Photonic Crystal Microcavities for High Throughput High Sensitivity Bio-Sensing on a Silicon-Chip Based Platform," Lab Chip 12, 2309 (2012).

[11] Zou, Y., Chakravarty, S., Wray, P., and Chen, R.T., "Mid-Infrared Holey and Slotted Photonic Crystal Waveguides in Silicon-on-Sapphire for Chemical Warfare Simulant Detection," Sensors and Actuators B 221, 1094 (2015)

[12] Zou, Y., Chakravarty, S., Wray, P., and Chen, R.T., "Experimental Demonstration of Propagation Characteristics of Mid-Infrared Photonic Crystal Waveguides in Silicon-on-Sapphire", Opt. Express 23, 6965 (2015).

[13] Zou, Y., H. Subbaraman, Chakravarty, S., Xu, X., Hosseini, A., Lai, W-C., Wray, P., and Chen, R.T., "Grating-coupled silicon-on-sapphire integrated slot waveguides operating at mid-infrared wavelengths," Optics Lett. 39, 3070 (2014)

[14] Mortensen, N.A., and Xiao, S.S., "Slow-light enhancement of Beer-Lambert-Bouguer absorption," Appl. Phys. Lett 90(14), 141108 (2007)

[15] Templin, M.F., Stoll,D., Schwenk, J.M., Potz, O., Kramer, S., and Joos, T.O., "Protein microarrays: Promising tools for proteomic research", Proteomics 3 (11), 2155 (2003).

[16] Schena, M., Shalon, D., Davis, R.W., and Brown, P.O., "Quantitative monitoring of gene-expression patterns with a complementary DNA microarray", Science 270 (5235), 467 (1995).

[17] Shalon, D., Smith, S.J., and Brown, P.O., "A DNA microarray system for analyzing complex DNA samples using two-color fluorescent probe hybridization", Genome Research 6 (7), 639 (1996).

[18] Falsey, J.R., Renil, M., Park, S., Lam, S.J., and Lam, K.S., "Peptide and small molecule microarray for high throughput cell adhesion and functional assays", Bioconjugate Chemistry 12 (3), 346 (2001).

[19] Wang, L., Li, P.C.H., Yu, H.Z., and Parameswaran, A.M., "Fungal pathogenic nucleic acid detection achieved with a microfluidic microarray device", Analytica Chimica Acta 610 (1), 97 (2008).

[20] Yang, C-J., Tang, N., Yan, H., Chakravarty, S., Li, D., and Chen, R.T., "193nm Lithography Fabricated High Sensitivity Photonic Crystal Microcavity Biosensors for Plasma Protein Detection in Patients with Pancreatic Cancer," in CLEO: 2015, OSA Technical Digest (online) (Optical Society of America, 2015), paper STu4K.5

[21] Yan, H., Yang, C-J., Zou, Y., Tang, N., Chakravarty, S., Chen, R.T., "Wide Dynamic Range Specific Detection of Therapeutic Drugs by Photonic Crystal Microcavity Arrays" in CLEO (Optical Society of America), Abstract ID: STu4K.2, San Jose, CA (2015)

[22] Yan, H., Tang, N., Chakravarty, S., Blake, D.A., and Chen RT., "High-sensitivity high-throughput chip based biosensor array for multiplexed detection of heavy metals" (submitted)

[23] de Feijter, J.A., Benjamins, J., Veer, F.A., "Ellipsometry as a tool to study the adsorption behavior of synthetic and biopolymers at the air–water interface", Biopolymers 17 (7), 1759 (1978).

[24] Voros, J., "The density and refractive index of adsorbing protein layers", Biophysical Journal 87 (1), 553 (2004).

[25] Chakravarty, S., Hosseini, A., Xu, X., Zhu, L., Zou, Y., and Chen, R. T., "Analysis of ultra-high sensitivity configuration in chip-integrated photonic crystal microcavity bio-sensors," Appl. Phys. Lett. 104, 191109 (2014).

[26] Lai, W-C., Chakravarty, S., Zou, Y., Guo, Y., and Chen, R. T., "Slow light enhanced sensitivity of resonance modes in photonic crystal biosensors," Appl. Phys. Lett. 102, 41111 (2013).

[27] Zou, Y., Chakravarty, S., Kwong, D.N., Lai, W-C., Xu, X., Lin, X., Hosseini, A., and Chen, R.T., "Cavity-Waveguide Coupling Engineered High Sensitivity Silicon Photonic Crystal Microcavity Biosensors with High Yield," IEEE Journal of Selected Topics in Quantum Electronics 20(4), 6900710 (2014).

[28] Chakravarty, S., Zou, Y., Lai, W-C., and Chen, R.T., "Slow light engineering for high Q high sensitivity photonic crystal microcavity biosensors in silicon," Biosensors and Bioelectronics 38(1), 170 (2012).

[29] Li, H., and Fan, X., "Characterization of sensing capability of optofluidic ring resonator biosensors", Appl. Phys. Lett. 97, 0111105 (2010).

[30] Barrios, C.A., "Optical slot-waveguide based biochemical sensors", Sensors 9(6), 4751 (2009).

[31] De Vos, K., Bartolozzi, I., Schacht, E., Bientsman, P., and Baets, R., "Silicon-on-Insulator microring resonator for sensitive and label-free biosensing", Opt. Exp. 15 (12), 7610 (2007).

[32] Carlborg, C.F., Gylfason, K.B., Kazmierczak, A., Dortu, F., Banuls Polo, M.J., Maquieira Catala, A., Kresbach, G.M., Sohlstrom, H., Moh, T., Vivien, L., Popplewell, J., Ronan, G., Barrios, C.A., Stemme, G., vander Woongaart, W., "A packaged optical slot-waveguide ring resonator sensor array for multiplex label-free assays in labs-on-chips", Lab on a Chip 10, 281 (2010).

[33] Dorfner, D., Zabel, T., Hurlimann, T., Hauke, N., Frandsen, L., Rant, U., Abstreiter, G., and Finley, J., "Photonic crystal nanostructures for optical biosensing applications", Biosensors and Bioelectronics 24, 2688 (2009).

[34] Mandal, S., Erickson, D., "Nanoscale optofluidic sensor arrays", Opt. Exp 16 (3): 1623 (2008).

[35] Zlatanovic, S., Mirkarimi, L.W., Sigalas, M.M., Bynum, M.A., Chow, E., Robotti, K.M., Burr, G.W., Esener, S., and Grot, A., "Photonic crystal microcavity sensor for ultracompact monitoring of reaction kinetics and protein concentration", Sensors and Actuators B: Chemical 141 (1), 13 (2009).

[36] Scullion, M.G., Di Falco, A., and Krauss, T.F., "Slotted photonic crystal cavities with integrated microfluidics for biosensing applications", Biosens. and Bioelectron. 27, 101 (2011).

[37] Kang, C., Phare, C.T., Vlasov, Y.A., Assefa, S., and Weiss S.M., "Photonic crystal slab sensor with enhanced surface area", Opt. Express 18(26), 27930 (2010).

[38] Lee, M., and Fauchet, P.M., "Two-dimensional silicon photonic crystal based biosensing platform for protein detection", Opt. Express 15, 4530 (2007)

[39] Cunningham, B.T., Li, P., Schulz, S., Lin, B., Baird, C., Gerstenmaier, J., Genick, C., Wang, F., Fine, E., and Laing, L., "Label-free assays on the BIND system", J. Biomolecular Screening 9, 481 (2004).